ACSNANO

www.acsnano.org

ARTICLE

Two-Dimensional $Bi_2Sr_2CaCu_2O_{8+\delta}$ Nanosheets for Ultrafast Photonics and Optoelectronics

Guanyu Liu,[#] Xiaozhi Bao,[#] Weikang Dong, Qi Wei, Haoran Mu, Wenguo Zhu, Bingzhe Wang, Jianding Li, Babar Shabbir, Yuan Huang, Guichuan Xing, Jianhui Yu, Peng Gao, Huaiyu Shao,* Xiangping Li,* and Qiaoliang Bao*

Cite This: *ACS Nano* 2021, 15, 8919–8929

Read Online

ACCESS | Metrics & More | Article Recommendations | Supporting Information

ABSTRACT: Two-dimensional (2D) $Bi_2Sr_2CaCu_2O_{8+\delta}$ (BSCCO) is a emerming class of 2D materials with high-temperature superconductivity for which their electronic transport properties have been intensively studied. However, the optical properties, especially nonlinear optical response and the photonic and optoelectronic applications of normal state 2D $Bi_2Sr_2CaCu_2O_{8+\delta}$ (Bi-2212), have been largely unexplored. Here, the linear and nonlinear optical properties of mechanically exfoliated Bi-2212 thin flakes are systematically investigated. 2D Bi-2212 shows a profound plasmon absorption in near-infrared wavelength range with ultrafast carrier dynamics as well as tunable nonlinear absorption depending on the thickness. We demonstrated that 2D Bi-2212 can be applied not only as an effective mode-locker for ultrashort pulse generation but also as an active medium for infrared light detection due to its plasmon absorption. Our results may trigger follow up studies on the optical properties of 2D BSCCO and demonstrate potential opportunities for photonic and optoelectronic applications.

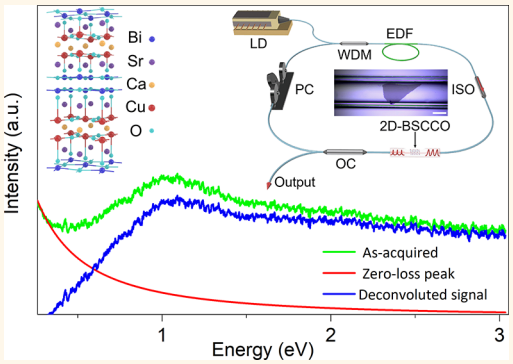

KEYWORDS: *BSCCO, nonlinear optical properties, plasmon absorption, mode-locking, photodetector*

INTRODUCTION

As a family of high-temperature superconductors, bismuth strontium calcium copper oxide (BSCCO) has a generalized chemical formula: $Bi_2Sr_2Ca_{n-1}Cu_nO_{2n+4+\delta}$, where $n = 1-3$. One of the most studied compounds is Bi-2212 with a chemical formula $Bi_2Sr_2CaCu_2O_{8+\delta}$, whereas $n = 2$.[1−4] The pseudogap,[5,6] infrared Hall angle,[7] and superconductivity[8] in bulk single crystal Bi-2212 have attracted intensive attention. Recently, exfoliated 2D Bi-2212 nanosheets have been used for exploring the role of dimensionality in high-temperature superconductivity. Superconductor−insulator transitions has been observed in thin films of lithium-intercalated 2D exfoliated Bi-2212 flakes.[9] A survey of monolayer Bi-2212 shows that doping concentration has less effect on the phases of superconductivity, charge order, pseudogap, and the Mott state, which are the same as those in the bulk, indicating the lack of the dimensionality effect.[10]

Many 2D materials including graphene, MXenes, and topological insulators (TIs) exhibit not only exotic electrical properties but also excellent optical properties, originating from their unique electronic band structures. For example, graphene has a special band structure with two Dirac cones meeting together at the Fermi level, which not only affords unusual electrical phenomena such as Klein tunneling[11,12] and an anomalous quantum Hall effect[13,14] but also gives rise to interesting optical responses like universal absorption constant,[15,16] tunable interband transitions,[17,18] and strong saturable absorption.[19,20] Bismuth-based TIs (e.g., Bi_2Te_3, Bi_2Se_3, and Sb_2Te_3) are insulating with a small bandgap in their interior, but their surfaces with single Dirac cone are conductive.[21,22] In terms of optical response, the TIs with small bandgaps have both broad-band linear[23] and nonlinear optical responses ranging from the UV to MIR region.[24−26] Recent research shows that 2D transition metal carbonitride MXenes are also suitable for photonic and optoelectronic applications due to their extraordinary nonlinear optical properties.[27,28] In addition, these 2D materials with exotic electrical properties and optical properties have also been extensively investigated for photodetectors in the past few

Received: February 21, 2021
Accepted: April 30, 2021
Published: May 10, 2021

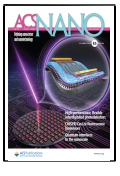

https://doi.org/10.1021/acsnano.1c01567
ACS Nano 2021, 15, 8919–8929

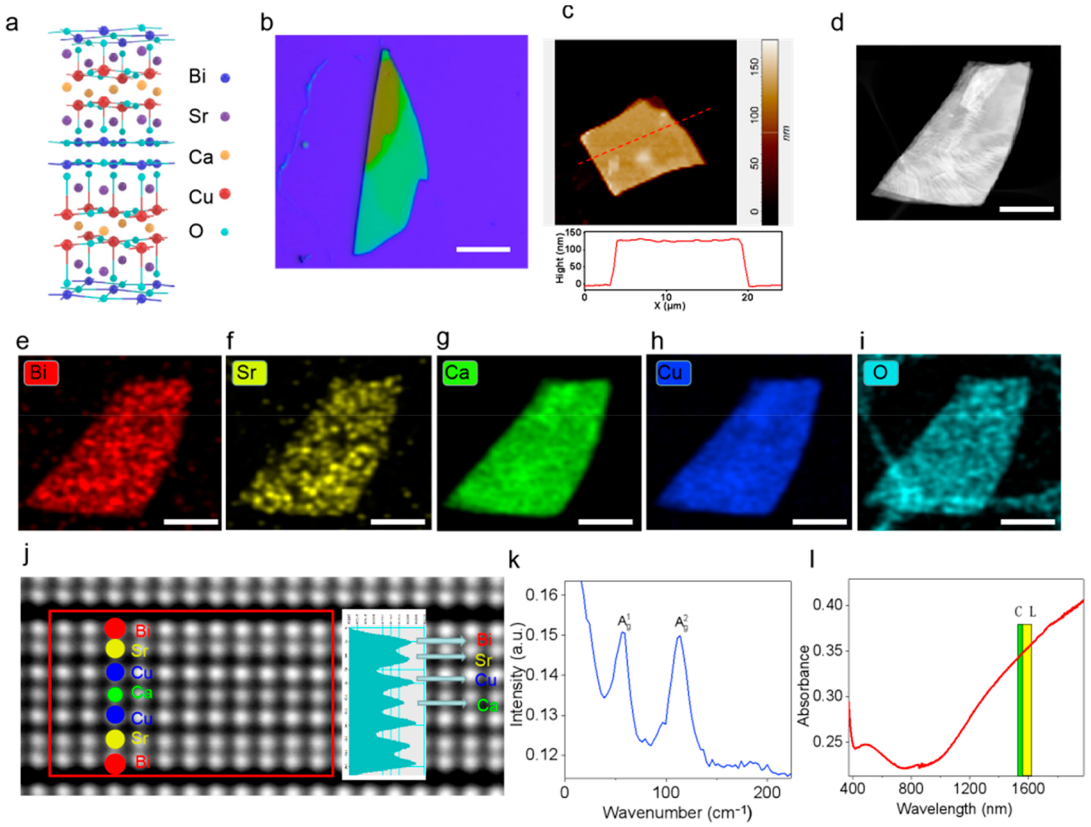

Figure 1. Physical characterization of BSCCO. (a) Schematic of the atomic structure of Bi-2212. (b) Optical image of an exfoliated Bi-2212 nanosheet on a Si/SiO_2 substrate. Scale bar: 20 μm. (c) AFM topography image of a Bi-2212 nanosheet (top panel) and cross-sectional height profile (bottom panel) along the dashed line in the topography image. (d) HAADF-STEM image of a Bi-2212 nanosheet. Scale bar: 500 nm. (e−i) EDS elemental map of the Bi, Sr, Ca, Cu, and O. Scale bar: 500 nm. (j) Atomically resolved HAADF-STEM image of the Bi-2212 nanosheet. Inset: the line-profile extracted from the red box on the left, presenting the different contrast of Bi, Sr, Ca, and Cu atom columns due to the different atomic numbers. (k) Raman spectrum of Bi-2212 nanosheet measured on SiO_2/Si substrate. The spectrum is excited by a 532 nm laser. (l) Linear absorption spectrum of Bi-2212 flake. The colored bars show the conventional (C) and long wavelength (L) telecommunication bands.

years.[29] In contrast, bulk Bi-2212 has very flat bands at the Fermi level[2] in its electronic structure, leading to many unusual physical properties such as anomalously high transition temperatures for superconductivity.[30] Whether the flat bands plus the dimensionality effect play key roles in unexplored optical phenomena in atomically thin layer Bi-2212 is an open question prompted by this curious fact, and if so, whether 2D Bi-2212 can be used as another emerging exotic material for optics and photonics. Previously, the optical absorption of bulk Bi-2212 has been measured to study the optical conductivity,[31] charge dynamics,[32] and optical anisotropy[33] in this material. However, the nonlinear optical response and the potential optoelectronic applications of normal state 2D Bi-2212 have never been reported, largely ignored in the research of their electronic properties.

In this work, the linear and nonlinear optical responses of mechanically exfoliated normal state Bi-2212 nanosheets are investigated and the photonic and optoelectronic applications in fiber-compatible devices are demonstrated. The 2D Bi-2212 crystal shows a resonant interband transition in the visible and a broad plasmon absorption at the near-infrared wavelength range. Spatially resolved electron energy-loss spectroscopy (EELS) and ultrafast femtosecond transient absorption spectroscopy of Bi-2212 nanosheets suggest that the near-infrared (NIR) optical response is associated with plasmon-assisted hot carriers. 2D Bi-2212 was utilized as a new mode-locker to generate picosecond pulses, benefiting from its ultrafast carrier dynamics and moderate nonlinear modulation depth. By integrating 2D Bi-2212 nanosheets onto the electrodes at the end-facet of a single silica fiber, we further demonstrate a highly fiber-compatible photodetector (FCPD) with a high photoresponsivity at telecommunication wavelength.

RESULTS AND DISCUSSION

The atomic structure of Bi-2212 is shown in Figure 1a. Bi-2212 crystals have a 2D layered lattice as other high-temperature superconductors in which CuO_2 planes are separated by double Bi_2O_2 layers. Similar to other 2D materials, multilayer Bi-2212 nanosheets can be produced by a mechanical exfoliation process.[34] Figure 1b shows the optical image of an exfoliated Bi-2212 nanosheet which was transferred onto a SiO_2/Si substrate. The topography of individual Bi-2212 nanosheets was investigated by atomic force microscopy (AFM). It is revealed that the surface of the exfoliated Bi-2212 sample is relatively smooth and the thickness is ~125 nm, as shown in Figure 1c. Figure 1d shows the high-angle annular dark field (HAADF) image of a Bi-2212 nanosheet which depicts relatively uniform contrast. The element distribution of Bi-2212 nanosheets was resolved by energy-dispersive spectroscopy (EDS) mapping and scanning transmission electron microscopy (STEM). Parts e−i of Figure 1

https://doi.org/10.1021/acsnano.1c01567
ACS Nano 2021, 15, 8919−8929

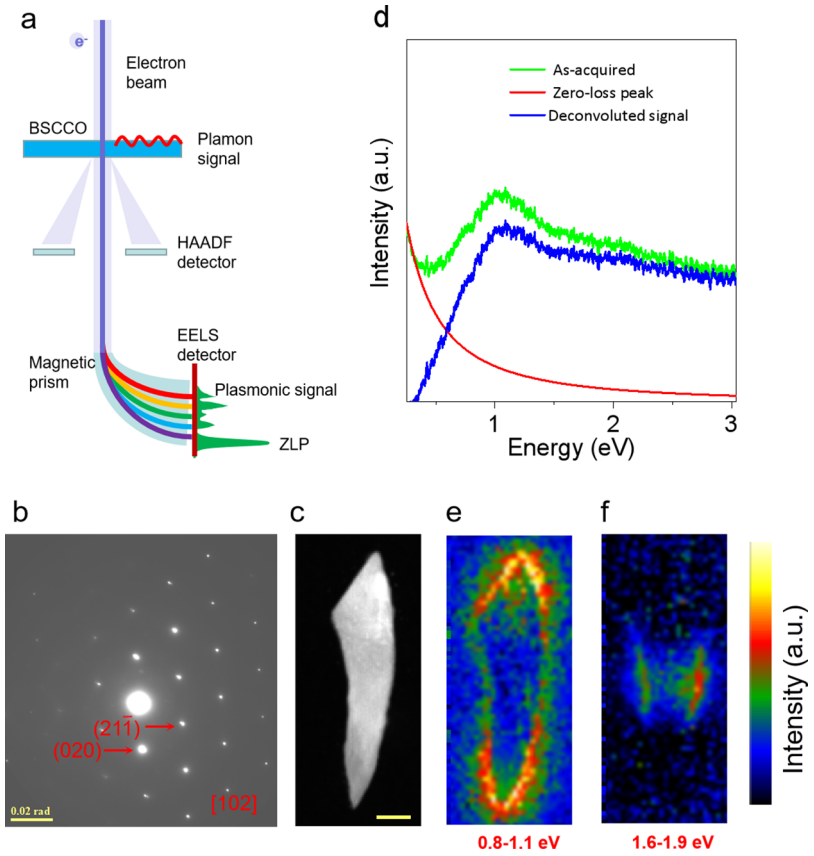

Figure 2. Plasmon signal of 2D Bi-2212 detected by STEM-EELS. (a) Schematic illustration of STEM-EELS system. (b) SAED pattern along the [102] direction. Scale bar: 0.02 rad. (c) HAADF image of a Bi-2212 nanosheet for EELS experiments. Scale bar: 50 nm. (d) EEL spectra taken in aloof geometry. Green trace, as-acquired spectrum to show the real signal which contains zero-loss peak; red trace, fitted zero-loss peak which is subtracted from the green trace to extract the plasmon signal; blue trace, the deconvoluted plasmon signal. (e) EELS intensity map of the dipole longitudinal mode (0.8−1.1 eV). (f) EELS intensity map of the quadrupole longitudinal mode (1.6−1.9 eV).

show the elemental map of a Bi-2212 nanosheet. It is found that the elemental distribution of Bi, Sr, Ca, Cu, and O is uniform throughout the Bi-2212 nanosheet. Figure 1j shows a typical atomic-level HAADF-STEM image of 2D Bi-2212 nanosheets along the [100] axis, which clearly resolves the layered atomic structure as illustrated in the schematic (Figure 1a). The inset is the line profile extracted from the red solid line on the left, presenting the different contrast of Bi, Sr, Ca, and Cu atoms as they have different atomic numbers. Raman spectroscopy with excitation at 532 nm was performed to characterize the as-prepared Bi-2212 samples. Figure 1k shows the Raman spectrum of the Bi-2212 nanosheet. The Raman spectrum shows two characteristic peaks at 58.8 and 113.8 cm^{-1}, which are related to A_g^1 and A_g^2 vibration modes of Bi-2212.[35] Figure 1l shows the linear optical absorption spectrum of the 2D Bi-2212 nanosheets in visible to NIR range. The peak below 400 nm originates from interband transitions in the Bi_2O_2 layers. The charge transfer between the CuO_2 planes of Bi-2212 leads to the small peak at around 500 nm.[33,36] The absorption increases steadily from 1000 nm throughout the NIR wavelength range, and the long slope is normally considered as the plasma edge.[33,36] The fact that 2D Bi-2212 has a broadband linear optical absorption makes it a promising broadband optical material for photonic and optoelectronic applications.

The plasmonic behavior of Bi-2212 nanosheets was investigated by the electron energy loss spectroscopy (EELS) in STEM. The experimental setup of STEM-EELS is schematically illustrated in Figure 2a. The sample interacts with the atom-wide high energy electrons, which lose a small fraction of their kinetic energy for launching surface plasmons. The information on surface plasmon properties can be extracted via the energy loss of plasma energy range. Meanwhile, accurate information about atomic structure or sample morphology can be obtained by the HAADF image. Figure 2b shows the selected area electron diffraction (SAED) pattern along the [102] zone axis where the lattice facet (020) and (21$\bar{1}$) can be resolved. A HAADF image of a ∼300 nm long wedge Bi-2212 nanosheet with an average width of ∼60 nm is depicted in Figure 2c. A typical EELS spectrum (the green curve) and a zero loss peak (ZLP) background (the red curve) with energy resolution ∼36 meV are shown in Figure 2d. After background subtraction, we obtain a broad plasmon resonance from 0.5 to 2.5 eV (blue curve in Figure 2d), which can be deconvoluted into a few components. Particularly, the first one is a conspicuous peak at ∼1.0 eV, which can be assigned to plasmon resonance originated from free electrons and bound electrons according to previous report.[37] A very weak peak ranging from 1.6 to 1.9 eV is also revealed. The discrepancy between the plasmon resonance from the optical measurements and that from EELs may result from the distortion gaps or local inhomogeneities in the stoichiometry of the sample.[38] Parts e and f of Figure 2 show the EELS intensity maps integrated at two peaks of the spectrum, respectively. It is found that the signal at 0.8−1.1 eV appears at

https://doi.org/10.1021/acsnano.1c01567
ACS Nano 2021, 15, 8919−8929

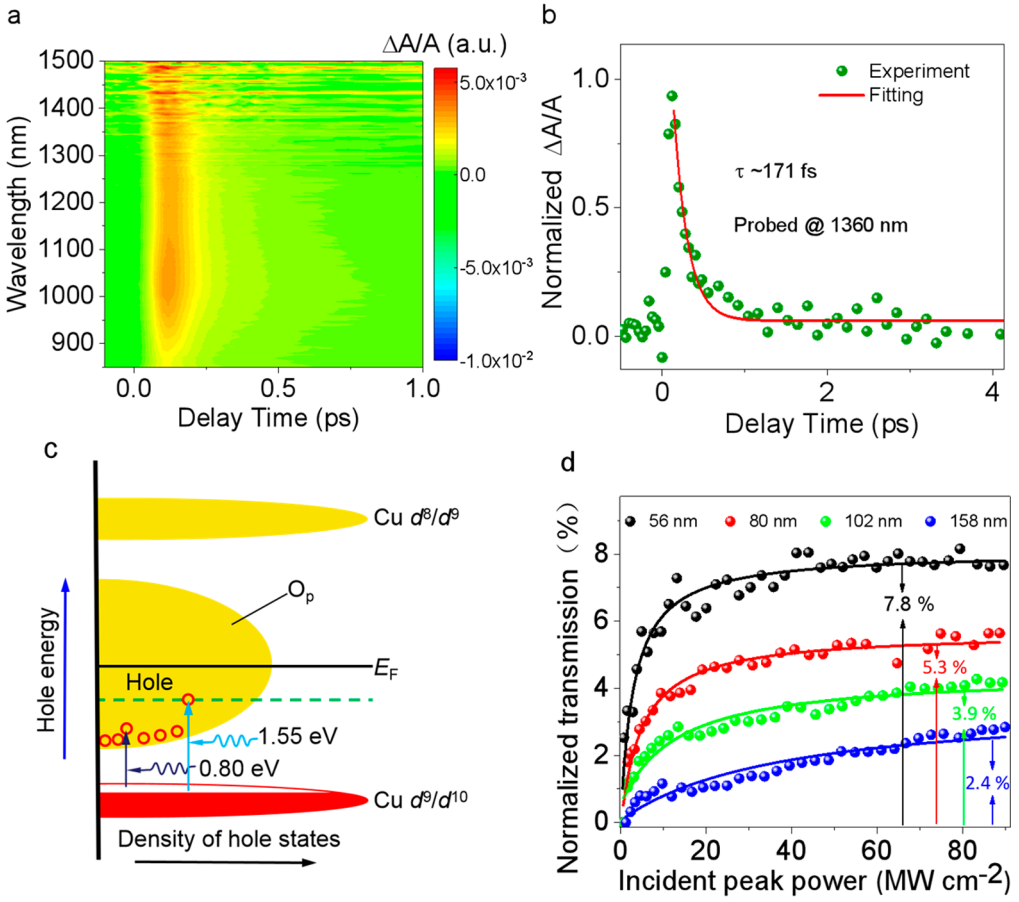

Figure 3. (a) Pseudo color NIR-region transient absorption spectra pumped at 800 nm. (b) Kinetic trace probed at 1360 nm. (c) Schematic illustration of energy states of light absorption present in the Cu−O planes. Hole energy is upward because the charge carriers in high-T_c superconductors are holes. The position of the O_p band is between the two Cu *d* bands, the d^8/d^9 band has no holes, but the d^9/d^{10} band is full of holes; the position of the Fermi level is somewhere in the O_p band, its exact position is not known. (d) Nonlinear transmission of Bi-2212 flakes with different thicknesses. The experimental data are analytically fitted by using eq 1.

two corners (tips) of the wedge nanosheet and the signal at 1.6−1.9 eV appears at two edges along long axis. The high energy dissipation of the EELS spectrum and the spatial harmonic distribution show that the free carrier oscillations along the lateral edges of the wedge Bi-2212 nanosheet are responsible for the multipolar longitudinal modes. We attribute the peaks at 0.8−1.1 and 1.6−1.9 eV to the dipole and quadrupole longitudinal modes of the surface plasmon supported by the Bi-2212 nanosheet, respectively, as those observed in metallic nanoribbons.[39,40]

The temperature-dependent carrier dynamics of normal-state cuprate superconductors at either 800 nm or the far-infrared range have been well studied in the past few years.[41−44] Nonequilibrium carrier dynamics in cuprate superconductors associated with plasmon absorption at room temperature have not been fully explored. Here, the carrier dynamics of plasmon resonance in normal-state 2D Bi-2212 nanosheets are investigated by ultrafast pump−probe experiments, as shown in Figure 3a,b. Pseduo color NIR-region transient absorption spectra pumped at 800 nm and probed at varying wavelengths from 850 to 1500 nm are shown in Figure 3a. It can be found that the carrier relaxation time depends linearly on the inverse of the probe photon energy (Figure S1, Supporting Information), which is consistent with previous studies[45] and similar to the results for graphene.[20,46] Figure 3b shows the measured absorptance transients with a probed wavelength of 1360 nm. The result is fitted by a single-component exponential decay function $\Delta A(t)/A = A_0 \exp(-t/\tau)$.[41,42] The carrier relaxation time τ of Bi-2212 is around 170 fs, which is on the same scale of that in graphene[19,20] and faster than those of widely studied 2D materials such as TMDs[47] and MXene.[48]

It is generally believed that the transient absorption response of Bi-2212 at room temperature results from the bolometric effect, which is similar to that in the metal,[41] i.e., the decay of transient absorption response results from thermalization process rather than recombination of the nonequilibrium carriers. In particular, the energy-dependent relaxation time described above (Figure S1) suggests that electron−plasmon interaction plays a more dominant role at the beginning. More specifically, after the laser pulse excites hot carriers, they thermalize among themselves. During this thermalization process, electron−electron collisions occur and lead to quasiparticle (i.e., plasmons) avalanche multiplication.[42] Then, the quasiparticles lose their energy to the lattice by emitting phonons. More specifically, the holes are excited to a copper oxygen p-like state from a d^9/d^{10}-like state by the incident pump light pulse and their excess energy heats the carriers in the metallic phase. This will lead to the opening states below (d^9/d^{10}-like states) and filling states above (oxygen *p*-like states), as shown in Figure 3c. An ultrafast rise of absorptance (written as $\Delta A/A$ which is the normalized

https://doi.org/10.1021/acsnano.1c01567
ACS Nano 2021, 15, 8919−8929

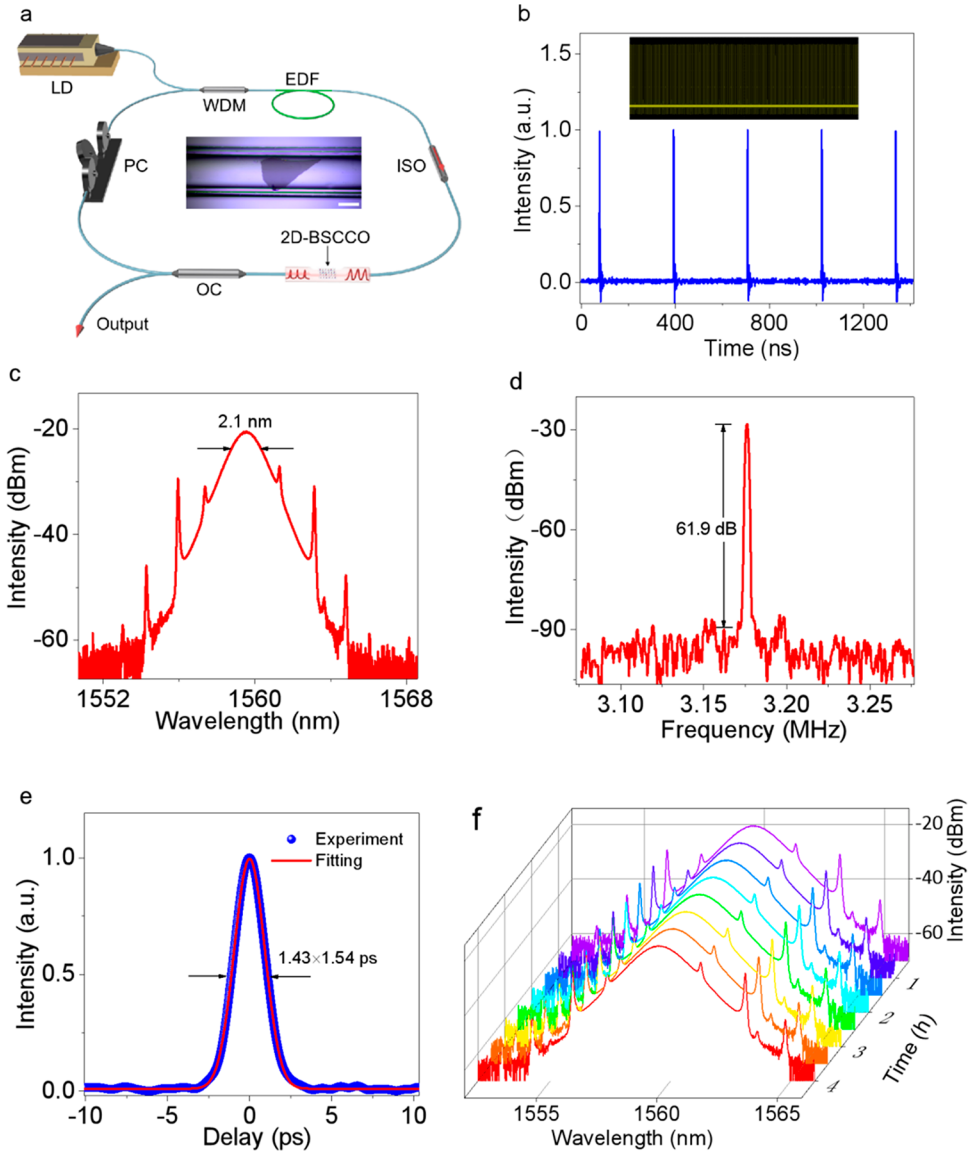

Figure 4. Typical characteristics of pulses output from the fiber laser based on 2D BSCCO flake mode locking. (a) Configuration of oscillator; LD: laser diode; PC: polarization controller; WDM: wavelength division multiplexer; EDF: erbium doped fiber; OC: optical coupler. Inset: photograph of Bi-2212 flake on side-polished fiber. Scale bar: 50 μm. (b) Pulse train of the output from the fiber laser. Inset: the wide-band oscilloscope tracings. (c) Typical mode-locking optical spectrum. The fwhm is 2.1 nm. (d) RF spectrum at the fundamental frequency. (e) Autocorrelation trace. (f) Measured time-dependent spectra of output pulse for over 4 h.

difference of absorption) suggests that pumping opens more states for absorption.[49] The absorptance drops to slowly decaying background which is associated with carrier-phonon coupling.

The Bi-2212 nanosheets were transferred onto the fiber end-facet (see insets of Figures S2b and S4a) or the side-polished fiber (SPF, inset of Figure 4a) for examining the nonlinear plasmon absorption of 2D Bi-2212. The nonlinear absorption of Bi-2212 was investigated by measuring the transmission of the SAs as a function of incident laser power at 1550 nm (see Figure S3 for details). The normalized nonlinear transmission curves of 2D Bi-2212 nanosheets on the end-facet of fiber ferrule with different thicknesses are shown in Figure 3d. The nonlinear transmission data collected above was normalized so that we can unambiguously compare the nonlinear modulation of the plasmon absorption. It clearly reveals that the transmissions of all the 2D Bi-22121 nanosheets increase dramatically within a particular incident laser intensity and then become saturated at higher intensity. This phenomenon is similar to the saturable absorption in graphene.[19] We may attribute the saturable absorption in 2D Bi-2212 to the diminishing of the available vacancy in oxygen p-like states (see Figure 3c). The nonlinear transmission curves can be fitted by[50]

$$T(I) = 1 - \frac{\alpha_s}{1 + I/I_s} - \alpha_{ns} \quad (1)$$

where $T(I)$, α_{ns}, α_s and I_s is the transmission of the SA, the nonsaturable absorption, the saturable absorption, and the saturable intensity, respectively. I_s is defined as the optical intensity that is required in a steady state to reduce the absorption to half of its unbleached value. Thicker Bi-2212 flakes not only have larger linear optical loss (Figure S3b) but also have larger nonlinear optical loss regime. The modulation

https://doi.org/10.1021/acsnano.1c01567
ACS Nano 2021, 15, 8919−8929

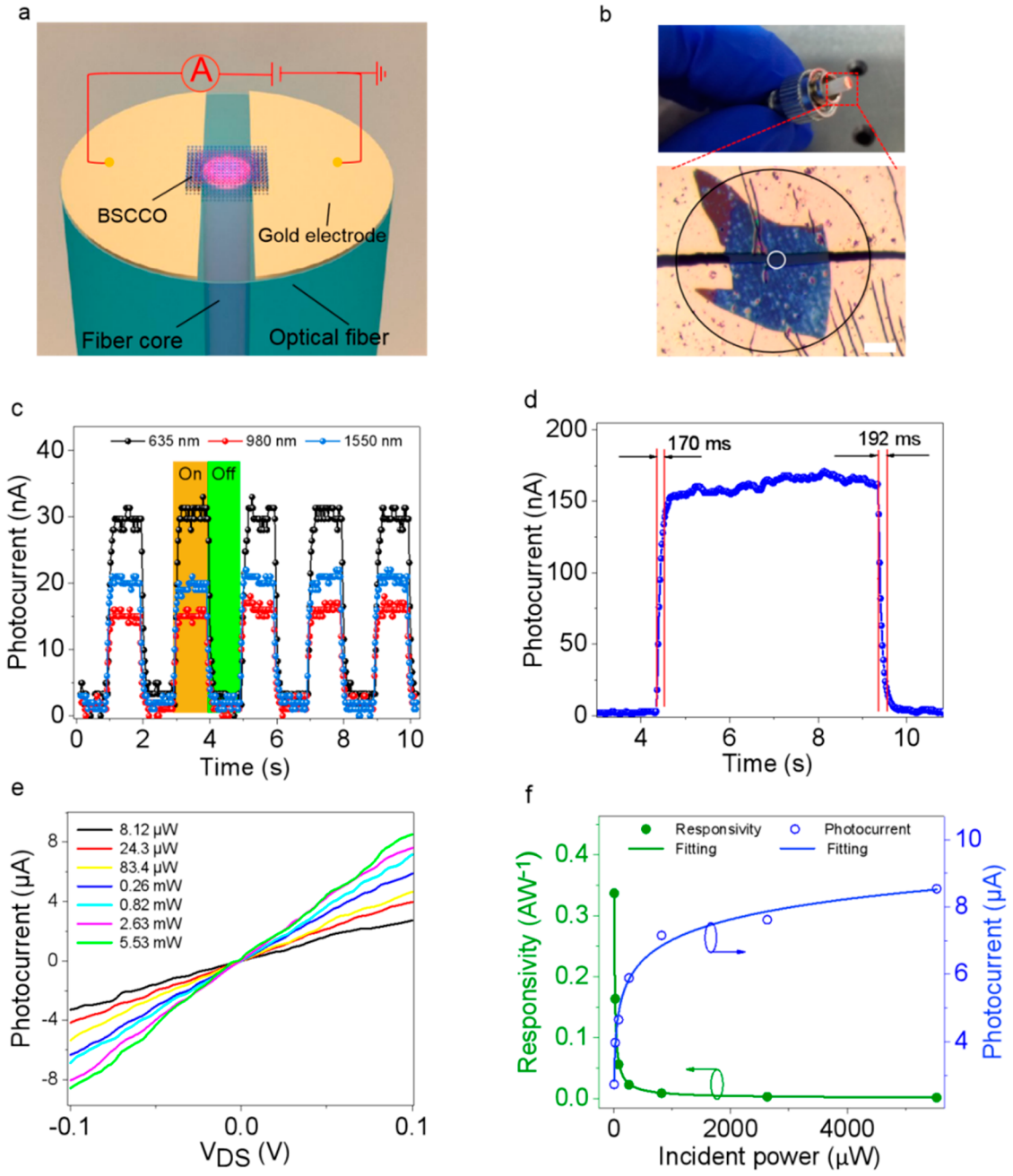

Figure 5. (a) Configuration of the fiber compatible photodetector. (b) Photograph (top panel) and optical microscope image (bottom panel) of the fabricated FCPD. The black and white circles in optical microscope image are 125 μm fiber cladding area and 9 μm fiber core, respectively. Scale bar: 20 μm. (c) Time-dependent photocurrent of the FCPD operating at 635, 980, and 1550 nm (V_{DS} = 0.1 mV). (d) Temporal photocurrent response at 1550 nm. V_{DS} = 0.1 mV. The rise time is 170 ms and the decay is 192 ms. (e) Bias voltage dependent photocurrent at different input light powers at 1550 nm. (f) Light power dependent responsivity and photocurrent of the FCPD at 1550 nm. V_{DS} = 100 mV. The lines are guides to eyes.

depth, which is defined as difference between saturable absorption transmission and linear absorption transmission, decreases from 7.8% to 2.4% with the thickness increasing from 56 to 158 nm. Enhanced scattering of multilayer Bi-2212 cause the increased nonsaturable loss, which leads to the decreased modulation depth while increasing the thickness. On the other hand, due to accumulated heat resulting from the enhanced absorption, a larger error has been observed in the analytical fit to the data of the thick sample (158 nm). We further measured the nonlinear transmission of the Bi-2212 on a SPF (Figure S3c). The SPF SA also exhibits characteristic behavior of saturable absorption; i.e., the transmission increases while the incident laser intensity increases and eventually flattens. The measured modulation depth is 2.9% and the saturation intensity is approximately 28 MW/cm^2, which is larger than that of few layer graphene[19] but smaller than that of MXene,[48] Bi_2Te_3,[51] and MoS_2.[52] These results suggest that Bi-2212 could be an ideal saturable absorber for ultrafast photonics.

The 2D Bi-2212-based SA devices were finally spliced into a ring cavity fiber laser, as shown in Figure 4a. Although the ultrashort pulses can be generated from the fiber laser by

https://doi.org/10.1021/acsnano.1c01567
ACS Nano 2021, 15, 8919−8929

placing 2D Bi-2212 SA on the cross-section of the fiber pigtail (see Figure S4), the laser generated noiselike pulses with low stability. Such mode-locking status can only maintain for about 30 min, which is likely caused by the thermal effect induced instability. In the case of 2D Bi-2212 SA integrated with SPF, the fiber laser is self-started when the pump power is increased up to 45 mW at appropriate polarization state. Typical mode-locking results are presented in Figure 4b–f. The output pulse train measured by an oscilloscope is shown in Figure 4b. The output pulse period is ~315 ns, corresponding to a cavity length of ~64.8 m. Figure 4c presents the spectrum of mode locked pulse with centered at 1559.5 nm and a full width at half-maximum (fwhm) of 2.1 nm. The symmetric Kelly can be observed in Figure 4c, suggesting a stable soliton state. The radio frequency (RF) spectrum of the output pulses is shown in Figure 4e. The repetition rate of the output pulse is ~3.17 MHz. Figure 4e shows the intensity autocorrelation (AC) trace of pulses output from the mode-locked fiber laser. The pulse duration is 1.43 ps. with $Sech^2$ profile assumed. The time-bandwidth product is 0.37 due to the slightly chirped output pulse. In order to verify the long-term operation of the cavity, we kept monitoring the spectra of the output pulse for over 4 h, as shown in Figure 4f. The spectra of output pulse at different times look almost the same. The laser can be self-started repeatably and running continuously over 4 h without observing of the break of the mode locking. The material did not degrade after the mode locking experiments and the laser can be also self-started even after several weeks. It is noteworthy that the performance of the 2D Bi-2212 based mode-locked fiber laser is comparable to those previous works with other 2D materials[50,53,54] (see Table S1). Using the SPF SA with larger 2D Bi-2212 nanosheets, stable Q-switched state can be achieved at a wide range pump power from 395 mW to 840 mW (Figure S5).

To explore the potential of 2D Bi-2212 for optoelectronic application, we fabricated a FCPD in which 2D Bi-2212 acts as channel material. Figure 5a shows a 3D schematic of the Bi-2212 FCPD. Two gold electrodes and a thin layer of Bi-2212 are directly transferred to the fiber end facet by a dry transfer method (see the Experimental section and section 6 in the Supporting Information for details). Figure 5b shows the photograph of a fiber pigtail with a fabricated FCPD (upper) and the optical microscope image of the FCPD (below) where the dark blue color area refers to the 2D Bi-2212 nanosheet.

We first investigate the wavelength-dependent optical response of Bi-2212 FCPD. Figure 5c shows time-dependent photocurrents ($I_{ph} = I_{light} - I_{dark}$) over five-period on–off operation at 635, 980, and 1550 nm for the incident power of 1 mW with a small bias voltage of 0.1 mV. It can be found that the switching function of the FCPD is effective and repeatable. Even though there is no obvious difference in the photoresponse time of the device at three different wavelengths, the photocurrent of the FCPD at 635 nm is much larger than that at 1550 nm and almost twice that at 980 nm. We attribute such a difference to different absorption mechanisms of 2D Bi-2212 at different wavelengths. Absorption of Bi-2212 at 635 nm is due to the interband transitions in the Bi_2O_2 layers, and the photon absorption generates extra electron–hole pairs, which have high energy and can be directly separated by a biasfield and collected by the electrodes. However, the absorption in the NIR range is caused by plasmon-assisted absorption which results from the coupling of photons and hot carriers.[55] We propose three consecutive steps for the photocurrent generation based on plasmon absorption in Bi-2212: first, the generation of energetic hot carriers upon the nonradiative attenuation of surface plasmon; second, some of the hot carriers can propagate across the Bi-2212 to the electrode before they lose their energy to the lattice by emitting phonons; last, the collection of photocarriers by the electrodes. Consequently, it is suggested that a larger photocurrent at 1550 nm as compared to that at 980 nm is due to stronger plamson coupling, which leads to more energetic hot carriers.

The rise time and decay time of photocurrent is ~170 and ~192 ms, respectively, as shown in Figure 5d. The power-dependent photocurrents at 1550 nm are plotted in Figure 5e. This indicates that the photocurrents increase linearly while increasing the bias voltage with a step length of 0.02 V. Photocurrents are observed only when the bias voltage (V_{DS}) is applied, which suggests the bias voltage drives the flow of carriers under illumination. The higher the light power, the more photons coupling with hot carriers, thus leading to more hot carriers that reach the electrodes, and giving to a larger photocurrent. Figure 5f shows the incident light dependent photocurrent and photoresponsivity of the 2D Bi-2212 based FCPD operating at 1550 nm under the bias voltage of 0.1 V. The photocurrent first increases nearly linearly with the increase of incident light power and then reaches to a constant at high power. This is because of the increased collisions between bounded photons and electrons. The relationship between the photocurrent I_{ph} and the light power P_{in} can be analytically fitted by using the equation $I_{ph} = aP_{in}^{b} + c$ where a, b, and c are the fitting parameters. The photoresponsivity of the FCPD is defined as the ratio of photocurrent to incident light power: $R = I_{ph}/P_{in}$. The photoresponsivity decreases while increasing the incident light power, which is similar to our previous reports on other 2D materials such as $MoTe_2$ and SnTe.[56,57] The photoresponsivity is up to 0.34 AW^{-1} under a low incident light power of 8.12 μW (V_{DS} = 0.1 V). It can be expected that a larger bias voltage or a lower incident power may achieve a higher photoresponsivity. It should be noted that the 2D Bi-2212 nanosheet is not stable for long time under ambient conditions, which caused those fluctuations in the electrical signals (see Figure 5e). The stability of the FCPD could be further improved by encapsulating the device and performing the fabrication as well as measurements in an inert environment. In comparison to conventional IR photodetectors based on silicon and semiconductor substrates, the FCPD demonstrated here can be easily connected to optical communication networks seamlessly for real-time monitoring the optical signals in the fiber.

CONCLUSION

In summary, we have investigated the optical properties, especially nonlinear optical properties, of 2D Bi-2212 nanosheets and demonstrated their application for ultrafast photonics and optoelectronics. A broadband plasmon absorption from the visible to NIR range was observed in normal state 2D Bi-2212, which has ultrafast carrier dynamics of 170 fs. The nonlinear transmission measurements of normal state Bi-2212 reveal that the thinner Bi-2212 nanosheet has a larger modulation depth. We demonstrated that 2D Bi-2212 is an effective SA for mode-locked fiber laser. Picosecond pulses were generated from a Er-doped fiber laser based on 2D Bi-2212 mode locking. We further fabricated a fiber-compatible photodetector using 2D Bi-2212 and achieved a considerably

https://doi.org/10.1021/acsnano.1c01567
ACS Nano 2021, 15, 8919–8929

high photoresponsivity of 0.34 AW^{-1} at 0.1 V upon light illumination at telecommunication band. Without any conventional lithographic process, the 2D Bi-2212-based FCPD represents a cost-effective solution for in-line photodetection in optical fiber systems. By elemental doping or ionic gating, one may expect to further tune the optical property in terms of plasmon resonance in BSCCO which deserves further investigation. Our work demonstrates potential opportunities for 2D BSCCO in ultrafast photonics and optoelectronics.

EXPERIMENTAL SECTION

Characterizations of 2D Bi-2212. All measurements and experimental operation are performed at room temperature to make sure that 2D Bi-2212 flakes are in normal state. Scotch tape was used to mechanically exfoliate 2D Bi-2212 nanosheets from bulk Bi-2212 single crystals (2D Semiconductor Co., USA). 2D Bi-2212 nanosheets were placed onto SiO_2/Si substrate, cross-section of fiber pigtail and the side polished fiber by dry transfer method for device fabrication and all optical characterizations. Optical images of 2D Bi-2212 samples were captured by using a conventional optical microscope (Olympus, BX53, Olympus Co.). An AFM (Ntegra solaris, NT-MDT Spectrum Instruments, Moscow, Russia) was used to investigate the topography and thickness of 2D Bi-2212 nanosheets. The Raman spectrum was measured by a micro-Raman system (WITec, Alpha 300R) with the excitation of 532 nm. The large size samples are transferred onto SiO_2 substrate by gold-assisted mechanical exfoliation method[58] and used for UV−vis−infrared absorption spectroscopy measurements (V-750, JASCO Co.). The EDS and atomically resolved STEM-HAADF images were acquired at an aberration-corrected FEI Themis Z microscope at 300 kV with beam current of 50 pA, a convergence semi-angle of 21 mrad, and a collection semi-angle snap in 39−200 mrad.

EELS Data Acquisition and Processing. A Nion Ultra STEMTM 200 microscope was used for the EELS data acquirement, with attached aberration correctors and a monochromator. The electron beam was set to 60 keV with energy resolution about ∼32 meV at the 15-mrad in beam convergence semiangle and 24.4 mrad in collection semiangle, and the spectrometer entrance aperture was set to 1 mm. The 3D EELs signal mapping time was set as 200 ms per pixel to reduce noise. Nion Swift software was used to acquire all EELS data. For the energy slight shift in collecting information on the ZLP, we aligned the spectrum by cross correlation; we then reduced the influence of beam current fluctuation through the integrated intensity of the unsaturated part of the ZLP, and the real signal spectrum was merged for all 2D spital dimensions on the maps.

Pump−Probe and Nonlinear Absorption Measurements. The transient absorption spectra were measured by the Helios instrument. The pump pulse (coherent Libra, 800 nm, 50 fs, 4 mJ) was generated by introducing 800 nm light into the optical parameter amplifier (OPerA Solo). The 800 nm fs pulse is passed through a 1 cm sapphire plate to generate a probe pulse in the near-infrared range (840−1600 nm). To measure the power-dependent nonlinear absorption, ∼4.8 ps, 40 MHz pulses output from a mode-locked fiber laser operating at wavelength of 1550 nm were amplified by a, erbium-doped fiber fiber (EDFA), and then the light is divided into two patch cords by a coupler for sample characterizations.

Passively Mode-Locked Fiber Laser Configuration. The gain fiber of the ring cavity was a piece of 1.1 m EDF (ESF-7/125, Nufern) which had an absorption coefficient of 24 dBm^{-1} at 976 nm. The other fiber was a 64.8 m long single mode fiber (SMF) which had a group velocity dispersion GVD parameter of 18 (ps/nm)/km. A 980/1550 nm pump wavelength division multiplexer (WDM) was employed to couple pump light into the fiber cavity. A polarization controller in the cavity was utilized to optimize the birefringence of the fiber. The laser output was extracted from the 10% port of the 90:10 coupler. The polarization independent isolator in the cavity played a role of forcing the unidirectional operation of the cavity. In addition, the cavity was pumped by a 980 nm laser diode with maximum power of 840 mW.

FCPD Fabrication and Characterizations. The FCPD was fabricated by a dry transfer method. Initially, a gold film (thickness: ∼50 nm) was deposited on the SiO_2substrate and then attached to the polydimethylsiloxane (PDMS) stamp. A suitable gap structure could be found and transferred onto the fiber end facet under a microscope (see section 6 of the Supporting Information for details). After that, we transferred the 2D Bi-2212 nanosheets onto the two electrodes and aligned them to make sure the whole fiber core area was covered by the sample. The fabrication process was performed under optical microscopy with the help of a high precision moving stage.

A source meter (Keithley 2450) was utilized to measure the photodetection characterizations at visible-NIR region on a probe station at room temperature in the open air. The illuminated light was directly projected to the FCPD at the output port of fiber without using any lens systems, which is different from that for a conventional field-effect transistor on silicon. A double-arm configuration is used to calibrate the input light power passing through the FCPD (see section 6, Supporting Information, for details).

ASSOCIATED CONTENT

Supporting Information

The Supporting Information is available free of charge at https://pubs.acs.org/doi/10.1021/acsnano.1c01567.

Pump−probe measurements, SA device fabrication, nonlinear absorption measurements, mode-locking using Bi-2212 on the fiber end-facet, Q-switching state characterizations, FCPD fabrication, and characterization (PDF)

AUTHOR INFORMATION

Corresponding Authors

Huaiyu Shao − *Joint Key Laboratory of the Ministry of Education, Institute of Applied Physics and Materials Engineering, University of Macau, Macau SAR 999078, China;* orcid.org/0000-0001-9286-7071; Email: hshao@um.edu.mo

Xiangping Li − *Guangdong Provincial Key Laboratory of Optical Fiber Sensing and Communications, Institute of Photonics Technology, Jinan University, Guangzhou 510632, China;* orcid.org/0000-0003-0955-2613; Email: xiangpingli@jnu.edu.cn

Qiaoliang Bao − *Department of Materials Science and Engineering, and ARC Centre of Excellence in Future Low-Energy Electronics Technologies, Monash University, Clayton, Victoria 3800, Australia;* orcid.org/0000-0002-6971-789X; Email: qiaoliang.bao@gmail.com

Authors

Guanyu Liu − *Guangdong Provincial Key Laboratory of Optical Fiber Sensing and Communications, Institute of Photonics Technology, Jinan University, Guangzhou 510632, China*

Xiaozhi Bao − *Joint Key Laboratory of the Ministry of Education, Institute of Applied Physics and Materials Engineering, University of Macau, Macau SAR 999078, China*

Weikang Dong − *International Center for Quantum Materials, and Electron Microscopy Laboratory, School of Physics, Peking University, Beijing 100871, China*

Qi Wei − *Joint Key Laboratory of the Ministry of Education, Institute of Applied Physics and Materials Engineering, University of Macau, Macau SAR 999078, China*

Haoran Mu − *Department of Materials Science and Engineering, and ARC Centre of Excellence in Future Low-Energy Electronics Technologies, Monash University, Clayton, Victoria 3800, Australia*

Wenguo Zhu − *Key Laboratory of Optoelectronic Information and Sensing Technologies of Guangdong Higher Educational Institutes, Jinan University, Guangzhou 510632, China;* orcid.org/0000-0002-9797-4201

Bingzhe Wang − *Joint Key Laboratory of the Ministry of Education, Institute of Applied Physics and Materials Engineering, University of Macau, Macau SAR 999078, China*

Jianding Li − *Joint Key Laboratory of the Ministry of Education, Institute of Applied Physics and Materials Engineering, University of Macau, Macau SAR 999078, China*

Babar Shabbir − *Department of Materials Science and Engineering, and ARC Centre of Excellence in Future Low-Energy Electronics Technologies, Monash University, Clayton, Victoria 3800, Australia;* orcid.org/0000-0002-2149-5546

Yuan Huang − *Institute of Physics, Chinese Academy of Sciences, Beijing 100190, China*

Guichuan Xing − *Joint Key Laboratory of the Ministry of Education, Institute of Applied Physics and Materials Engineering, University of Macau, Macau SAR 999078, China;* orcid.org/0000-0003-2769-8659

Jianhui Yu − *Key Laboratory of Optoelectronic Information and Sensing Technologies of Guangdong Higher Educational Institutes, Jinan University, Guangzhou 510632, China*

Peng Gao − *International Center for Quantum Materials, and Electron Microscopy Laboratory, School of Physics, Peking University, Beijing 100871, China*

Complete contact information is available at: https://pubs.acs.org/10.1021/acsnano.1c01567

Author Contributions

[#]G.L. and X.B. contributed equally to this work.

Notes

The authors declare no competing financial interest.

ACKNOWLEDGMENTS

This work was supported by the National Key Research & Development Program of China (Nos. 2016YFA0201902 and 2018YFB1107200), Guangdong Provincial Innovation and Entrepreneurship Project (No. 2016ZT06D081), the Shenzhen Nanshan District Pilotage Team Program (No. LHTD20170006), the Macau Science and Technology Development Fund (FDCT No. 0062/2018/A2, 0019/2019/AGJ, FDCT-091/2017/A2, and FDCT-014/2017/AMJ), Research Grants (MYRG2019-00055-IAPME) from University of Macau and the Natural Science Foundation of China (No. 91733302, 61605073, 61904152, 11974023, 52021006, and 61935017), the National Key Research and Development Program of China (Grant Nos. 2019YFA0308000 and 2018YFA0704201), the Strategic Priority Research Program (Grant No. XDB33000000) and Natural Science Foundation of Guangdong Province (Grant No. 2021A1515010694).

REFERENCES

(1) Brunel, L. C.; Louie, S. G.; Martinez, G.; Labdi, S.; Raffy, H. Superconducting Gap in $Bi_2Sr_2CaCu_2O_8$. *Phys. Rev. Lett.* **1991**, *66*, 1346−1349.

(2) Dessau, D. S.; Shen, Z. X.; King, D. M.; Marshall, D. S.; Lombardo, L. W.; Dickinson, P. H.; Loeser, A. G.; DiCarlo, J.; Park, C.-H.; Kapitulnik, A.; Spicer, W. E. Key Features in the Measured Band Structure of $Bi_2Sr_2CaCu_2O_{8+\delta}$: Flat Bands at E_F and Fermi Surface Nesting. *Phys. Rev. Lett.* **1993**, *71*, 2781−2784.

(3) Kim, J.-T.; Chung, S. H.; Ha, D. H.; Yoo, K.-H.; Park, Y. K.; Park, J.-C.; Kim, M.-S.; Lee, S.-I. Critical Dynamics Of Superconducting $Bi_2Sr_2CaCu_2O_8$ Single Crystal. *IEEE Trans. Magn.* **1999**, *35*, 4082−4084.

(4) Hamidian, M. H.; Edkins, S. D.; Joo, S. H.; Kostin, A.; Eisaki, H.; Uchida, S.; Lawler, M. J.; Kim, E.-A.; Mackenzie, A. P.; Fujita, K.; Lee, J.; Davis, J. C. S. Detection of a Cooper-Pair Density Wave in $Bi_2Sr_2CaCu_2O_{8+}x$. *Nature* **2016**, *532*, 343−347.

(5) Watanabe, T.; Fujii, T.; Matsuda, A. Pseudogap in $Bi_2Sr_2CaCu_2O_{8+\delta}$Studied by Measuring Anisotropic Susceptibilities and Out-of-Plane Transport. *Phys. Rev. Lett.* **2000**, *84*, 5848−5851.

(6) Vershinin, M.; Misra, S.; Ono, S.; Abe, Y.; Ando, Y.; Yazdani, A. Local Ordering in the Pseudogap State of the High-Tc Superconductor $Bi_2Sr_2CaCu_2O_{8+\delta}$. *Science* **2004**, *303*, 1995−1998.

(7) Jenkins, G. S.; Schmadel, D. C.; Sushkov, A. B.; Gu, G. D.; Kontani, H.; Drew, H. D. Terahertz Hall Measurements on Optimally Doped Single-Crystal $Bi_2Sr_2CaCu_2O_{8+}x$. *Phys. Rev. B: Condens. Matter Mater. Phys.* **2010**, *82*, 094518.

(8) Pushp, A.; Parker, C. V.; Pasupathy, A. N.; Gomes, K. K.; Ono, S.; Wen, J.; Xu, Z.; Gu, G.; Yazdani, A. Extending Universal Nodal Excitations Optimizes Superconductivity in $Bi_2Sr_2CaCu_2O_{8+\delta}$. *Science* **2009**, *324*, 1689−1693.

(9) Liao, M.; Zhu, Y.; Zhang, J.; Zhong, R.; Schneeloch, J.; Gu, G.; Jiang, K.; Zhang, D.; Ma, X.; Xue, Q.-K. Superconductor−Insulator Transitions in Exfoliated $Bi_2Sr_2CaCu_2O_{8+\delta}$ Flakes. *Nano Lett.* **2018**, *18*, 5660−5665.

(10) Yu, Y.; Ma, L.; Cai, P.; Zhong, R.; Ye, C.; Shen, J.; Gu, G. D.; Chen, X. H.; Zhang, Y. High-Temperature Superconductivity in Monolayer $Bi_2Sr_2CaCu_2O_{8+\delta}$. *Nature* **2019**, *575*, 156−163.

(11) Katsnelson, M. I.; Novoselov, K. S.; Geim, A. K. Chiral Tunnelling and the Klein Paradox in Graphene. *Nat. Phys.* **2006**, *2*, 620−625.

(12) Young, A. F.; Philip, K. Quantum Interference and Klein Tunnelling in Graphene Heterojunctions. *Nat. Phys.* **2009**, *5*, 222−226.

(13) Novoselov, K. S.; Geim, A. K.; Morozov, S. V.; Jiang, D.; Katsnelson, M. I.; Grigorieva, I. V.; Dubonos, S. V.; Firsov, A. A. Two-Dimensional Gas of Massless Dirac Fermions in Graphene. *Nature* **2005**, *438*, 197−200.

(14) Zhang, Y.; Tan, Y.-W.; Stormer, H. L.; Kim, P. Experimental Observation of the Quantum Hall Effect and Berry's Phase in Graphene. *Nature* **2005**, *438*, 201−204.

(15) Mak, K. F.; Sfeir, M. Y.; Wu, Y.; Lui, C. H.; Misewich, J. A.; Heinz, T. F. Measurement of the Optical Conductivity of Graphene. *Phys. Rev. Lett.* **2008**, *101*, 196405.

(16) Nair, R. R.; Blake, P.; Grigorenko, A. N.; Novoselov, K. S.; Booth, T. J.; Stauber, T.; Peres, N. M. R.; Geim, A. K. Fine Structure Constant Defines Visual Transparency of Graphene. *Science* **2008**, *320*, 1308.

(17) Li, Z. Q.; Henriksen, E. A.; Jiang, Z.; Hao, Z.; Martin, M. C.; Kim, P.; Stormer, H. L.; Basov, D. N. Dirac Charge Dynamics in Graphene by Infrared Spectroscopy. *Nat. Phys.* **2008**, *4*, 532−535.

(18) Wang, F.; Zhang, Y.; Tian, C.; Girit, C.; Zettl, A.; Crommie, M.; Shen, Y. R. Gate-Variable Optical Transitions in Graphene. *Science* **2008**, *320*, 206−209.

(19) Bao, Q.; Zhang, H.; Yang, J.-X.; Wang, S.; Tang, D. Y.; Jose, R.; Ramakrishna, S.; Lim, C. T.; Loh, K. P. Graphene−Polymer Nanofiber Membrane for Ultrafast Photonics. *Adv. Funct. Mater.* **2010**, *20*, 782−791.

(20) Bao, Q.; Zhang, H.; Ni, Z.; Wang, Y.; Polavarapu, L.; Shen, Z.; Xu, Q.-H.; Tang, D.; Loh, K. P. Monolayer Graphene as a Saturable Absorber in a Mode-Locked Laser. *Nano Res.* **2011**, *4*, 297−307.
(21) Peng, H.; Lai, K.; Kong, D.; Meister, S.; Chen, Y.; Qi, X.-L.; Zhang, S.-C.; Shen, Z.-X.; Cui, Y. Aharonov−Bohm Interference in Topological Insulator Nanoribbons. *Nat. Mater.* **2010**, *9*, 225−229.
(22) Xiu, F.; He, L.; Wang, Y.; Cheng, L.; Chang, L.-T.; Lang, M.; Huang, G.; Kou, X.; Zhou, Y.; Jiang, X.; Chen, Z.; Zou, J.; Shailos, A.; Wang, K. L. Manipulating Surface States in Topological Insulator Nanoribbons. *Nat. Nanotechnol.* **2011**, *6*, 216−221.
(23) Peng, H.; Dang, W.; Cao, J.; Chen, Y.; Wu, D.; Zheng, W.; Li, H.; Shen, Z.-X.; Liu, Z. Topological Insulator Nanostructures for Near-Infrared Transparent Flexible Electrodes. *Nat. Chem.* **2012**, *4*, 281−286.
(24) Zhao, C.; Zhang, H.; Qi, X.; Chen, Y.; Wang, Z.; Wen, S.; Tang, D. Ultra-Short Pulse Generation by a Topological Insulator Based Saturable Absorber. *Appl. Phys. Lett.* **2012**, *101*, 211106.
(25) Giorgianni, F.; Chiadroni, E.; Rovere, A.; Cestelli-Guidi, M.; Perucchi, A.; Bellaveglia, M.; Castellano, M.; Giovenale, D. D.; Pirro, G. D.; Ferrario, M.; Pompili, R.; Vaccarezza, C.; Villa, F.; Cianchi, A.; Mostacci, A.; Petrarca, M.; Brahlek, M.; Koirala, N.; Oh, S.; Lupi, S. Strong Nonlinear Terahertz Response Induced by Dirac Surface States in Bi_2Se_3 Topological Insulator. *Nat. Commun.* **2016**, *7*, 11421.
(26) Wang, Y.; Liu, S.; Yuan, J.; Wang, P.; Chen, J.; Li, J.; Xiao, S.; Bao, Q.; Gao, Y.; He, J. Ultra-broadband Nonlinear Saturable Absorption for Two-Dimensional $Bi_2Te_xSe_{3-x}$ Nanosheets. *Sci. Rep.* **2016**, *6*, 33070.
(27) Jhon, Y. I.; Koo, J.; Anasori, B.; Seo, M.; Lee, J. H.; Gogotsi, Y.; Jhon, Y. M. Metallic MXene Saturable Absorber for Femtosecond Mode-Locked Lasers. *Adv. Mater.* **2017**, *29*, 1702496.
(28) Jhon, Y. I.; Seo, M.; Jhon, Y. M. First-Principles Study of a MXene Terahertz Detector. *Nanoscale* **2018**, *10*, 69−75.
(29) Zheng, K.; Luo, L.-B.; Zhang, T.-F.; Liu, Y.-H.; Yu, Y.-Q.; Lu, R.; Qiu, H.-L.; Li, Z.-J.; Andrew Huang, J. C. Optoelectronic Characteristics of a Near Infrared Light Photodetector Based on a Topological Insulator Sb_2Te_3 Film. *J. Mater. Chem. C* **2015**, *3*, 9154−9160.
(30) Herman, F.; Kasowski, R. V.; Hsu, W. Y. Electronic Structure of $Bi_2Sr_2CaCu_2O_8$ High-Tc Superconductors. *Phys. Rev. B: Condens. Matter Mater. Phys.* **1988**, *38*, 204.
(31) Reedyk, M.; Bonn, D. A.; Garrett, J. D.; Greedan, J. E.; Stager, C. V.; Timusk, T.; Kamarás, K.; Tanner, D. B. Far-Infrared Optical Properties of $Bi_2Sr_2CaCu_2O_8$. *Phys. Rev. B: Condens. Matter Mater. Phys.* **1988**, *38*, 11981.
(32) Tu, J. J.; Homes, C. C.; Gu, G. D.; Basov, D. N.; Strongin, M. Optical Studies of Charge Dynamics in Optimally Doped $Bi_2Sr_2CaCu_2O_{8+\delta}$. *Phys. Rev. B: Condens. Matter Mater. Phys.* **2002**, *66*, 144514.
(33) Quijada, M. A.; Tanner, D. B.; Kelley, R. J.; Onellion, M.; Berger, H.; Margaritondo, G. Anisotropy in the *ab*-Plane Optical Properties of $Bi_2Sr_2CaCu_2O_8$ Single-Domain Crystals. *Phys. Rev. B: Condens. Matter Mater. Phys.* **1999**, *60*, 14917.
(34) Novoselov, K. S.; Jiang, D.; Schedin, F.; Booth, T. J.; Khotkevich, V. V.; Morozov, S. V.; Geim, A. K. Two-Dimensional Atomic Crystals. *Proc. Natl. Acad. Sci. U. S. A.* **2005**, *102*, 10451−10453.
(35) Kirillov, D.; Bozovic, I.; Geballe, T. H.; Kapitulnik, A.; Mitzi, D. B. Raman Scattering Spectra of Superconducting $Bi_2Sr_2CaCu_2O_8$ Single Crystals. *Phys. Rev. B: Condens. Matter Mater. Phys.* **1988**, *38*, 11955.
(36) Liu, H. L.; Quijada, M. A.; Zibold, A. M.; Yoon, Y.-D.; Tanner, D. B.; Cao, G.; Crow, J. E.; Berger, H.; Margaritondo, G.; Forró, L.; O, B.-H.; Markert, J. T.; Kelly, R. J.; Onellion, M. Doping-Induced Change of Optical Properties in Underdoped Cuprate Superconductors. *J. Phys.: Condens. Matter* **1999**, *11*, 239.
(37) Nücker, N.; Eckern, U.; Fink, J.; Müller, P. Long-Wavelength Collective Excitations of Charge Carriers in High-Tc Superconductors. *Phys. Rev. B: Condens. Matter Mater. Phys.* **1991**, *44*, 7155.
(38) Wang, Y. Y.; Feng, G.; Ritter, A. L. Electron-Energy-Loss and Optical-Transmittance Investigation of $Bi_2Sr_2CaCu_2O_8$. *Phys. Rev. B: Condens. Matter Mater. Phys.* **1990**, *42*, 420.
(39) Brongersma, M. L.; Kik, P. G. *Surface Plasmon Nanophotonics*; Springer: New York, 2007.
(40) Zhu, Y.-P.; El-Demellawi, J. K.; Yin, J.; Lopatin, S.; Lei, Y.; Liu, Z.; Miao, X.; Mohammed, O. F.; Alshareef, H. N. Unprecedented Surface Plasmon Modes in Monoclinic MoO_2 Nanostructures. *Adv. Mater.* **2020**, *32*, 1908392.
(41) Liu, Y. H.; Toda, Y.; Shimatake, K.; Momono, N.; Oda, M.; Ido, M. Direct Observation of the Coexistence of the Pseudogap and Superconducting Quasiparticles in $Bi_2Sr_2CaCu_2O_{8+y}$ by Time-Resolved Optical Spectroscopy. *Phys. Rev. Lett.* **2008**, *101*, 137003.
(42) Kabanov, V. V.; Demsar, J.; Podobnik, B.; Mihailovic, D. Quasiparticle Relaxation Dynamics in Superconductors with Different Gap Structures: Theory and Experiments on $YBa_2Cu_3O_{7-\delta}$. *Phys. Rev. B: Condens. Matter Mater. Phys.* **1999**, *59*, 1497.
(43) Kaindl, R. A.; Woerner, M.; Elsaesser, T.; Smith, D. C.; Ryan, J. F.; Farnan, G. A.; Mccurry, M. P.; Walmsley, D. G. Ultrafast Mid-Infrared Response of $YBa_2Cu_3O_{7-\delta}$. *Science* **2000**, *287*, 470−473.
(44) Albrecht, W.; Kruse, Th.; Kurz, H. Time-Resolved Observation of Coherent Phonons in Superconducting $YBa_2Cu_3O_{7-\delta}$ Thin Films. *Phys. Rev. Lett.* **1992**, *69*, 1451.
(45) Olson, C. G.; Liu, R.; Lynch, D. W.; List, R. S.; Arko, A. J.; Veal, B. W.; Chang, Y. C.; Jiang, P. Z.; Paulikas, A. P. High-Resolution Angle-Resolved Photoemission Study of the Fermi Surface and the Normal-State Electronic Structure of $Bi_2Sr_2CaCu_2O_8$. *Phys. Rev. B: Condens. Matter Mater. Phys.* **1990**, *42*, 381.
(46) Xu, S.; Cao, J.; Miller, C. C.; Mantell, D. A.; Miller, R. J. D.; Gao, Y. Energy Dependence of Electron Lifetime in Graphite Observed with Femtosecond Photoemission Spectroscopy. *Phys. Rev. Lett.* **1996**, *76*, 483.
(47) Cui, Q.; Ceballos, F.; Kumar, N.; Zhao, H. Transient Absorption Microscopy of Monolayer and Bulk WSe_2. *ACS Nano* **2014**, *8*, 2970−2976.
(48) Dong, Y.; Chertopalov, S.; Maleski, K.; Anasori, B.; Hu, L.; Bhattacharya, S.; Rao, A. M.; Gogotsi, Y.; Mochalin, V. N.; Podila, R. Saturable Absorption in 2D Ti_3C_2 MXene Thin Films for Passive Photonic Diodes. *Adv. Mater.* **2018**, *30*, 1705714.
(49) Brorson, S. D.; Kazeroonian, A.; Face, D. W.; Cheng, T. K.; Doll, G. L.; Dresselhaus, M. S.; Dresselhaus, G.; Ippen, E. P.; Venkatesan, T.; Inam, A. Femtosecond Thermomodulation Study of High-Tc Superconductors. *Solid State Commun.* **1990**, *74*, 1305−1308.
(50) Tuo, M.; Xu, C.; Mu, H.; Bao, X.; Wang, Y.; Xiao, S.; Ma, W.; Li, L.; Tang, D.; Zhang, H.; Premaratne, M.; Sun, B.; Cheng, H.-M.; Li, S.; Ren, W.; Bao, Q. Ultrathin 2D Transition Metal Carbides for Ultrafast Pulsed Fiber Lasers. *ACS Photonics* **2018**, *5*, 1808−1816.
(51) Mu, H.; Wang, Z.; Yuan, J.; Xiao, S.; Chen, C.; Chen, Y.; Chen, Y.; Song, J.; Wang, Y.; Xue, Y.; Zhang, H.; Bao, Q. Graphene−Bi_2Te_3 Heterostructure as Saturable Absorber for Short Pulse Generation. *ACS Photonics* **2015**, *2*, 832.
(52) Zhang, H.; Lu, S. B.; Zheng, J.; Du, J.; Wen, S. C.; Tang, D. Y.; Loh, K. P. Molybdenum Disulfide (MoS_2) as a Broadband Saturable Absorber for Ultra-Fast Photonics. *Opt. Express* **2014**, *22*, 7249−7260.
(53) Mu, H.; Lin, S.; Wang, Z.; Xiao, S.; Li, P.; Chen, Y.; Zhang, H.; Bao, H.; Lau, S. P.; Pan, C.; Fan, D.; Bao, Q. Black Phosphorus−Polymer Composites for Pulsed Lasers. *Adv. Opt. Mater.* **2015**, *3*, 1447−1453.
(54) Xia, H.; Li, H.; Lan, C.; Li, C.; Zhang, X.; Zhang, S.; Liu, Y. Ultrafast Erbium-Doped Fiber Laser Mode-Locked by a CVD-Grown Molybdenum Disulfide (MoS_2) Saturable Absorber. *Opt. Express* **2014**, *22*, 17341−17348.
(55) Velusamy, D. B.; El-Demellawi, J. K.; El-Zohry, A. M.; Giugni, A.; Lopatin, S.; Hedhili, M. N.; Mansour, A. E.; Fabrizio, E. D.; Mohammed, O. F.; Alshareef, H. N. MXenes for Plasmonic Photodetection. *Adv. Mater.* **2019**, *31*, 1807658.

https://doi.org/10.1021/acsnano.1c01567
ACS Nano 2021, 15, 8919−8929

(56) Yu, W.; Li, S.; Zhang, Y.; Ma, W.; Sun, T.; Yuan, J.; Fu, K.; Bao, Q. Near-Infrared Photodetectors Based on $MoTe_2$/Graphene Heterostructure with High Responsivity and Flexibility. *Small* **2017**, *13*, 1700268.
(57) Yang, J.; Yu, W.; Pan, Z.; Yu, Q.; Yin, Q.; Guo, L.; Zhao, Y.; Sun, T.; Bao, Q.; Zhang, K. Ultra-Broadband Flexible Photodetector Based on Topological Crystalline Insulator SnTe with High Responsivity. *Small* **2018**, *14*, 1802598.
(58) Huang, Y.; Pan, Y.-H.; Yang, R.; Bao, L.-H.; Meng, L.; Luo, H.-L.; Cai, Y.-Q.; Liu, G.-D.; Zhao, W.-J.; Zhou, Z.; Wu, L.-M.; Zhu, Z.-L.; Huang, M.; Liu, L.-W.; Liu, L.; Cheng, P.; Wu, K.-H.; Tian, S.-B.; Gu, C.-Z.; Shi, Y.-G.; et al. Universal Mechanical Exfoliation of Large-Area 2D Crystals. *Nat. Commun.* **2020**, *11*, 2453.

https://doi.org/10.1021/acsnano.1c01567
ACS Nano 2021, 15, 8919−8929